JOURNAL OF SPACECRAFT AND ROCKETS
Vol. 45, No. 4, July–August 2008

Static Aeroelastic Analysis of Thin-Film Clamped Ballute for Titan Aerocapture

Reuben R. Rohrschneider*
Ball Aerospace & Technologies Corporation, Boulder, Colorado 80301
and
Robert D. Braun†
Georgia Institute of Technology, Atlanta, Georgia 30332-0150

DOI: 10.2514/1.33350

Many authors have shown the potential mass savings that a ballute can offer for both aerocapture and entry. This mass savings could enhance or even enable many scientific and human exploration missions. Before the flight of a ballute, several technical issues need to be addressed, including aeroelastic behavior. This paper addresses the issue of aeroelastic behavior by developing an analysis framework and performing a validation effort that uses wind-tunnel tests of clamped ballute models constructed of Kapton supported by a rigid nose and floating aft ring. Good correlation is obtained using modified Newtonian aerodynamics and nonlinear structural analysis with temperature-dependent material properties and thermal expansion. This analysis framework is then used to compute the deformed shape of a clamped ballute for Titan aerocapture in both the continuum and transitional regimes using impact method aerodynamics, computational fluid dynamics, and direct simulation Monte Carlo.

Nomenclature

A	=	area of a surface element, m^2
B	=	constant in bridging function
C_p	=	pressure coefficient
C_z	=	axial force coefficient.
E	=	Young's modulus, GPa
Kn	=	Knudsen number
m	=	log base in bridging function
$nbmin$	=	minimum number of flow cells on the body
P	=	pressure on a surface element, Pa
q	=	dynamic pressure, Pa
T	=	temperature
γ	=	ratio of specific heats
λ	=	mean free path
ν	=	Poisson ratio

Subscripts

bridge	=	bridged value in the transitional regime
cont	=	continuum regime value
fm	=	free-molecular regime value

I. Introduction

THE concept of the ballute has been around since the early 1960s and was first proposed for aerocapture in 1981 [1,2]. These initial ballutes were constructed of coated fabrics and often required flexible thermal protection. A significant breakthrough was made by McRonald when he discovered that increasing the ballute size to obtain a ballistic coefficient of 1 kg/m^2 or less would decrease the heat rate to an order of 1 W/cm^2, at which point polymer materials could be used to construct the ballute [3]. This advance was made possible by materials developed in the 1980s and led to a resurgence of interest in ballutes. In [4], Rohrschneider and Braun explored the current state of the art and technology gaps were identified in the areas of radiative heating and aeroelastic analysis. Hall also concluded that coupled analysis is necessary when analyzing ballutes [5].

This paper begins to address the requirement for coupled analysis of ballutes and fully automates the coupling of nonlinear structural analysis and hypersonic aerodynamics in the continuum, rarefied, and transitional regimes. The coupled code is validated using wind-tunnel tests performed by the In-Space Propulsion group at NASA Marshall Space flight Center, and shows good agreement when temperature-dependent material properties and thermal expansion effects are included. Finally, a ballute for Titan aerocapture is analyzed in the continuum regime at the peak dynamic pressure point on the trajectory and in the transitional regime.

II. Ballute Aeroelastic Analysis Tool

Coupling of aeroelastic problems can be divided into loosely coupled methods [6] which allow use of existing codes with little or no modification, and monolithic or fully integrated methods [7] which require a complete code rewrite.

Loosely coupled methods typically use existing analysis codes, rely on input and output files for data transfer, and do not necessarily exchange data at the end of each aerodynamic or structural dynamic analysis time step [8]. This allows for use of validated codes, substitution of other analysis codes, and simple coupling through the use of boundary conditions. Monolithic methods start with the governing equations of the problem and solve them simultaneously using a custom-built solution algorithm. This requires a reformulation of the governing equations for compatibility [9], and because the source code is typically written in-house, tweaking is possible but validation is much more difficult.

The loose coupling method has been chosen for this application due in part to time constraints, lower complexity, and the desire to use validated codes. The method is also more modular and can be adapted more easily for variations on the problem and advances made in each discipline's analysis.

The analysis of thin-film ballutes requires structural dynamics and aerothermodynamics in the rarefied, transitional, and continuum regime. Existing tools were chosen where available to eliminate the need to fully validate each individual analysis code. For all analyses a text file interface and command line execution are required for ease of integration into the interface code. Alternatively, analyses

Received 9 July 2007; accepted for publication 9 December 2007.

*Systems Engineer, Spacecraft Subsystems. Member AIAA.
†David and Andrew Lewis Professor of Space Technology, Guggenheim School of Aerospace Engineering. Associate Fellow AIAA.

developed for this project can be run as subfunctions to the interface code, allowing data passing through memory.

A. Structural Analysis

The structural dynamics analysis needs to analyze geometrically nonlinear deformation of thin polymer films with temperature-dependent material properties. Several commercial codes were evaluated. LS-DYNA [10] performed the best and produced consistent answers where other codes encountered numerical stability problems. Solutions to thin-film problems in LS-DYNA are straightforward, requiring few additional inputs to achieve stability. The resulting displacement, velocity, and acceleration are produced at the nodes and temperatures and shear forces are input at nodes, while pressures are input at element face centers.

To ensure that the proper parameters are used in LS-DYNA for the coupled problem, an inflated column buckling problem was computed and compared to experimental results published by Topping [11]. The experiment that most closely represents a thin-film ballute construction is a 0.0005-in. thick Mylar column inflated to 4.89 psi. Several element formulations and material models were used in LS-DYNA in an attempt to find the best modeling parameters for thin inflated membrane structures.

The buckling load from experiment was found to be 5.45 lb by Topping and most of the element and material model combinations produced buckling loads between 5.28 and 5.37 lb. The notable exception is the membrane model which produces buckling loads of 8.76 lb, much higher than the experimentally observed value. This is likely due to the inability of the membrane model to produce a moment which initiates buckling in the numerical model. Because of the fast run time, the fabric model with 10% liner thickness is used when thermal effects are not being considered.

B. Aerodynamic Analysis

Continuum aerodynamics will be calculated by NASCART-GT [12,13] which is capable of handling flow chemistry in the hypersonic flight regime. Various equation sets are available including Navier–Stokes, Euler, or modified Newtonian and the analysis can run on multiple processors. NASCART-GT uses a Cartesian grid and the only required geometric input is a triangulated surface. Currently, all analysis assumes an inviscid perfect gas.

DAC [14] will be used for the rarefied and transitional aerodynamics and was obtained from the Technology Transfer and Commercialization Office at NASA Johnson Space Center. The analysis is based on the direct simulation Monte Carlo (DSMC) method of Bird [15]. Flow chemistry is available if reaction equations are provided, but current analysis assumes a perfect gas. Furthermore, this method produces good solutions for any flow speed with high Knudsen number. DAC uses a Cartesian grid method with manually driven grid refinement based on the cell size to mean free path ratio. Grid refinement will be avoided by careful selection of the initial grid, due to difficulty in automating the refinement.

Because of the long computation time required by both NASCART-GT and DAC, a simplified set of aerodynamic tools is also being used. In the continuum regime, the modified Newtonian method [16] has been implemented, and in the rarefied regime the collisionless DSMC method [15] is used. The transitional regime is covered by use of a bridging function [17] of the form:

$$C_{p,\text{bridge}} = C_{p,\text{cont}} + (C_{p,\text{fm}} - C_{p,\text{cont}})\sin^2\left\{\pi\left[B + \left(\tfrac{1}{2} - B\right)\log_m(Kn)\right]\right\} \quad (1)$$

In Eq. (1), B and m are found by fitting the computational fluid dynamics (CFD) and DSMC results calculated by Gnoffo and Richard Wilmoth of NASA Langley Research Center for the toroidal trailing ballute at Titan [18]. Coefficients were found that minimized the square of the difference between the bridging function and the actual results. The continuum and rarefied limits were also allowed to vary. The resulting values for B, m, and the bounds are presented in Table 1. Of note is the low value of the continuum limiting Knudsen number which is 0.00049, lower than the typical limit of 0.001 [19].

Table 1 Optimized bridging function parameters

Parameter	Optimized value
B	0.436
m	3.044
Kn_{upper}	3.044
Kn_{lower}	0.00049

C. Boundary Condition Mapping

Coupling the analysis codes requires a scheme for transferring boundary condition data between the disparate analyses and, over time, the coupling scheme needs to introduce as little error as possible so that energy is not artificially dissipated, causing incorrect deformation.

LS-DYNA uses primarily four-node shell elements while DAC and NASCART-GT require a pure three-node shell element input. Both DAC and NASCART-GT only require surface resolution from the input grid, which can be satisfied by simply splitting the four-node elements from the LS-DYNA input. Unfortunately, NASCART-GT has proven unable to handle the high number of input cells required by the structures model, necessitating a second, coarser grid.

To couple LS-DYNA with DAC, the mixed triangular-quadrilateral grid used for structural analysis is split into a pure triangular grid. Because both the LS-DYNA and DAC grids use the same nodes, transferring displacement data is straightforward. Transferring pressure data from the aerodynamic grid to the structural dynamic grid requires area weighted averaging from two three-node elements to a single four-node element. Pressure transfer uses Eq. (2), with the nomenclature illustrated in Fig. 1,

$$P_{\text{quad}} = \frac{P_{\text{tri}_1}A_{\text{tri}_1} + P_{\text{tri}_2}A_{\text{tri}_2}}{A_{\text{tri}_1} + A_{\text{tri}_2}} \quad (2)$$

Here A is the area of a triangular element, and P is the pressure on the element specified by the subscript. This method ensures that total force magnitude is conserved when boundary data are transferred, but does not necessarily match force direction. Force direction should be close because the quadrilateral element should not twist very much in the structural analysis, and there is no way to match direction using pressure loading.

Coupling LS-DYNA with NASCART-GT requires that the triangular aerodynamic grid be coarsened when the structural grid is large, which is the case for the analysis presented in Sec. IV.D.1. Because the structural grid is produced by rotating a set of nodes about an axis, the coarse aerodynamic grid is generated by using every fifth node in the radial and circumferential directions of the structural grid. Because nodes match between the two models, transferring displacement data only requires knowledge of the matching node numbers. For transferring pressure data, structural elements are mapped to aerodynamic elements by proximity of the quadrilateral element centroid to the larger triangular element's

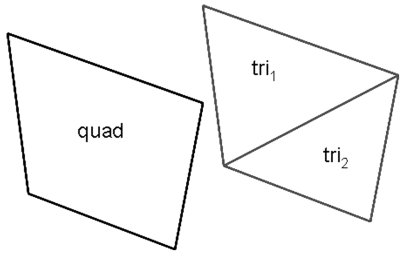

Fig. 1 Nomenclature for area weighted pressure averaging between the triangular aerodynamics grid and quadrilateral structures grid with matching nodes.

centroid. For simplicity, no interpolation or element cutting is performed when mapping elements. For a curved geometry, this leads to elements on the diagonal mapping to the triangle element with larger radius. A simple example of the element mapping for pressure transfer is shown in Fig. 2. In theory this leads to a bias toward the pressure of triangular elements at a larger radius, but in practice the difference in pressure between these two triangles is very small because NASCART-GT is interpolating pressure data from a Cartesian grid back to the triangular input grid, and the elements are small compared to the geometric features of the model.

III. Ballute Aeroelastic Analysis Tool Validation Study

Validation of thin-film structures in a hypersonic flight condition is difficult due to the limited data available. To date, only two relevant tests have been performed, and only one provided deformation profiles. The first test aimed to demonstrate that a thin-film polymer could survive hypersonic flight conditions and obtain deflection measurements of the membrane under load. The second test acquired qualitative temperature data on the membrane surface and would have provided quantitative temperature profiles, but testing and calibration was cut short due to funding issues. Because of these test limitations, a largely qualitative validation is performed in this section.

A. Geometry and Flight Conditions

Both tests were performed at the NASA Langley Research Center as part of NASA's In-Space Propulsion (ISP) program [20]. The first tests used both the hypersonic CF_4 tunnel and the 31-in. Mach 10 air tunnel, and the second test only used the Mach 10 air tunnel. This validation study selected run 15 (6-in. diam model, 1-mil Kapton membrane, CF_4 tunnel) from the first set of tests because it is the most flexible model tested, the shock structure is visible in the available photograph, and the dynamic pressure and heat rate are low. The low dynamic pressure should minimize thermal effects on material properties in these results, providing a better deformed shape validation opportunity.

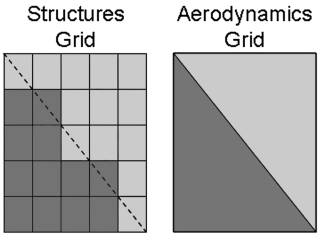

Fig. 2 Element mapping for pressure load transfer between the coarse NASCART-GT grid and the Fine LS-DYNA grid.

A clamped ballute configuration was tested, and was composed of a rigid nose and rigid outer support with a membrane stretched between. The outer support was allowed to float axially to allow for the axial deformation expected in flight. The outer diameter of the model was 15.24 cm and the rigid nose diameter was 1.3 cm. Figure 3 shows the test model before testing. The membrane is constructed of 0.254-mm (0.001-in.) thick Kapton and forms a 60-deg half-angle cone with one seam. During testing the seam was placed on the opposite side of the model from the camera so as to have the smallest affect on the results possible. Deformation data are from photographs of the model during testing, and no dynamic data are available. Figure 4 shows an example photograph of the deformed profile during testing and the wrinkle pattern observed after testing. Because membrane deformation remains after the loading is removed, one or more of creep, plasticity, or thermal setting phenomenon take place in the test model. None of these effects are captured in the computational analyses and so exact deformations cannot be reproduced, but qualitatively the deformed shape should be similar. Unfortunately, the model deforms further during the cooling process, so post-test photographs cannot be used to generate quantitative deformation profiles.

The test conditions are in the hypersonic flight regime, but do not match any specific point on a calculated ballute aerocapture trajectory at Titan due to wind tunnel and scaling limitations. Table 2 shows the test conditions and the flight conditions of a clamped ballute at peak dynamic pressure along a typical Titan ballute aerocapture trajectory. The test conditions have a higher dynamic pressure than the calculated ballute trajectory leading to larger forces on the test model. The larger aerodynamic force counters the higher stiffness of the test model compared to the flight article due to unavailability of Kapton less than 0.254 mm thick. The wind tunnels are not capable of matching the flight conditions exactly, but were run as close as possible to their limits while still ensuring correct results. The test Knudsen number is 0.00046, which is within the continuum regime, making this a useful validation case for the modified Newtonian method and NASCART-GT.

The test membrane is constructed of Kapton and was estimated to be at 260°C by the test engineer (Greg Buck of NASA Langley). Experimental data for the modulus of elasticity are available at 23, 200, and 500°C and were linearly interpolated to obtain the value at 260°C. At the estimated temperature the modulus is 1.479 GPa and the Poisson's ratio is 0.34 [21]. Because of the lack of temperature

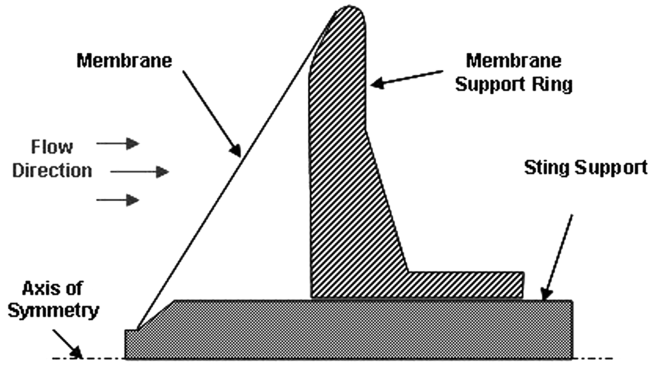

Fig. 3 A cross section of the CF_4 wind-tunnel test model before testing. Notice that the outer membrane support can move axially along the sting [20].

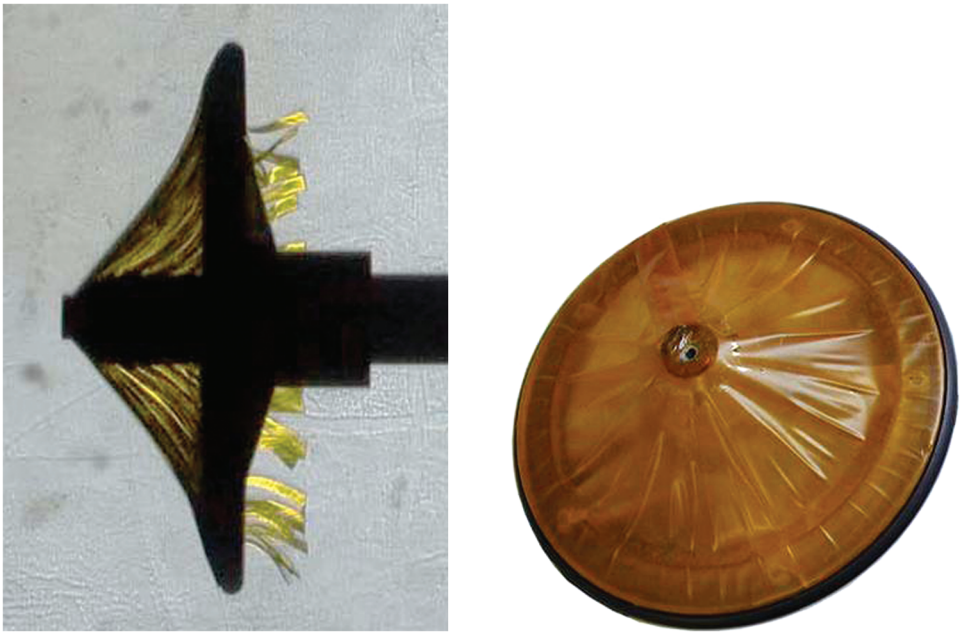

Fig. 4 The CF_4 wind-tunnel test model during testing (left) and after testing (right) [20].

data from the test, the surface temperature is assumed to be uniform over the membrane.

B. Structural Model and Grid Convergence Study

A finite element model was created of the wind-tunnel test article using quadrilateral elements. Only one-quarter of the model was used for computation due to the global symmetry of deformation and the local wrinkling of the surface. The membrane is modeled using the fabric material model with a 10% liner and the nose and aft support ring are assumed to be rigid. The model is fully constrained from the nose, and the aft ring is constrained radially.

The base model has 12 circumferential and 10 radial elements to simulate one-quarter of the membrane, resulting in a fairly coarse model. Four different refinement levels were made that increase the number of elements used to simulate the membrane from 120 up to 4992. Several solution metrics were tracked, including the number of surface wrinkles formed, the maximum principle stress, and the maximum axial deflection. Surface wrinkles are important in this model because they indicate buckling of the membrane due to a compressive stress in the hoop direction and they eliminate the ability to carry load in the hoop direction. Stroud and Zender [22] showed experimentally that conic-shaped shells buckle in the circumferential direction under a uniform pressure load, which produces surface wrinkles. The finite element analysis (FEA) model does not claim to capture the form of the wrinkles properly because bending is not included in the element formulation, but the load carrying ability in the circumferential direction is eliminated, which is important for the overall deformation. Figure 5 shows the deformed grid on each model and the number of elements used to model the membrane. For the finest grid, the number of circumferential elements is doubled as you move from the spacecraft outward. This was done to keep the minimum edge length at a reasonable size because smaller edges require small time steps and produce long run times. The structural models were run until a steady state was reached with a uniform pressure applied to the membrane (not coupled to aerodynamic analysis). Figure 6 shows that the Fine and XFine models have converged for both axial deflection and principle stress, but the number of wrinkles continues to bounce between 3 and 4. The variation in number of wrinkles between 3 and 4 does not appear to impact the displacement or stress significantly, and is likely due to the use of a quarter model. The angle between the wrinkles is approximately the same in the Fine and XFine models, indicating that the orientation relative to the quarter model has changed, but the number of wrinkles in a full model is the same. Further computations will use the Fine model.

Table 2 ISP CF_4 wind-tunnel test conditions and clamped ballute flight conditions at peak dynamic pressure at Titan

Parameter	CF_4 test	Clamped ballute at peak q on Titan
Dynamic pressure, Pa	654.0	51.5
Atm. density, kg/m^3	1.46×10^{-3}	5.66×10^{-6}
Atm. temperature, K	254.0	166.4
Velocity, m/s	945.0	4226.4
Sonic speed, m/s	168.0	259.9
Mach no.	5.6	16.4

C. Coupled Low-Fidelity Aerodynamics Solution

The low-fidelity aerodynamic code assumes a perfect gas and GasEQ [23] was used to determine the ratio of specific heats for the equilibrium flow properties of CF_4 at the freestream temperature of 254 K. The resulting ratio of specific heats is 1.176 and the gas constant is 94.47 J/kg · K. The coupled code was run for 6.5 s (13 iterations) at which point the solution had reached a steady state. The resulting deformed shape is shown in Fig. 7 with surface pressure contours. The quarter model used for computation was reflected twice to produce a complete model for visualization purposes. The large surface wrinkles observed in test (Fig. 4) are present, but the minor wrinkles between each major wrinkle are not as prominent. Figure 8 shows that the membrane contour matches well, within 0.3% for the inner third and within 3% for the outer third of the model where the floating support ring has moved forward in the computation and backward in the experiment. This difference indicates that the material must have a lower modulus (higher temperature) or expand substantially due to thermal effects. Membrane deformation in the experiment was hampered by interference with the support structure of the aft ring, but this is not expected to cause such a substantial difference in aft ring movement.

The discrepancy between the computed and experimental profiles in Fig. 8 is likely caused by incorrect material properties, incorrect pressure distribution, or thermal expansion. The pressure distribution produced by the low-fidelity aerodynamics does not take into account the complex shock structure observed around the body that will be addressed by using high-fidelity CFD analysis in the following section. Incorrect material properties could be due to either material nonlinearity or an incorrect estimate of the material

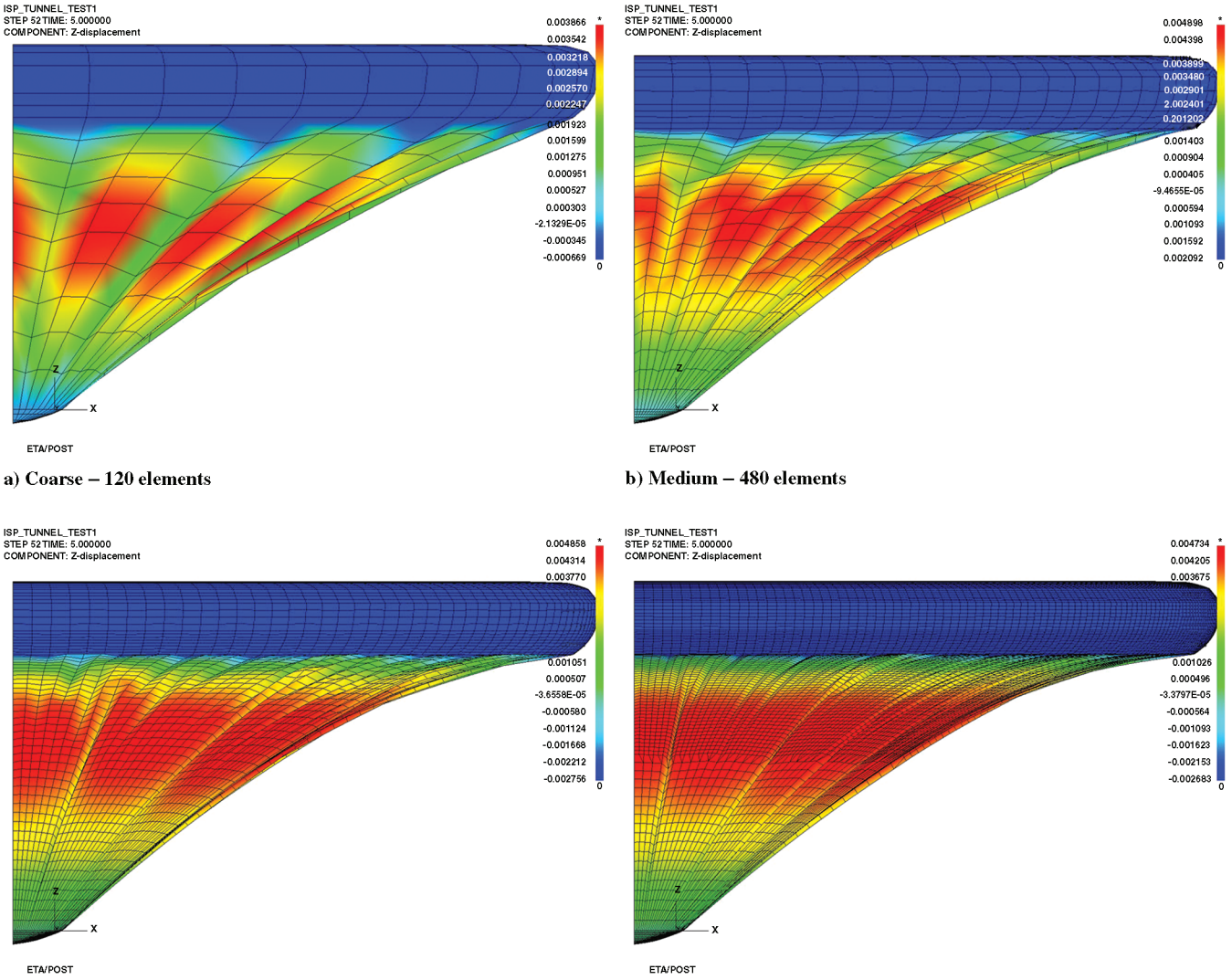

Fig. 5 Grids used in the convergence study of the ISP wind-tunnel test model; red indicates larger displacement.

temperature. Stress–strain profiles for Kapton 30HN at 500, 260, and 23°C are shown in Fig. 9. ILC Dover provided the data at 500°C [24] and the data at 200 and 23°C are from DuPont product literature [21]. The peak stress calculated for the test model is 22 MPa, which falls in the linear region of the stress–strain curve at both 23 and 200°C. Curves are interpolated between 200 and 500°C to estimate that the calculated peak stress of 21 MPa is still within the linear range of this material up to about 425°C. Because of the linear nature of the material in the temperature range explored, material nonlinearity does not account for the discrepancy.

Models were run at 350°C without thermal expansion and at 260°C with thermal expansion. Figure 10 shows the radial profile of

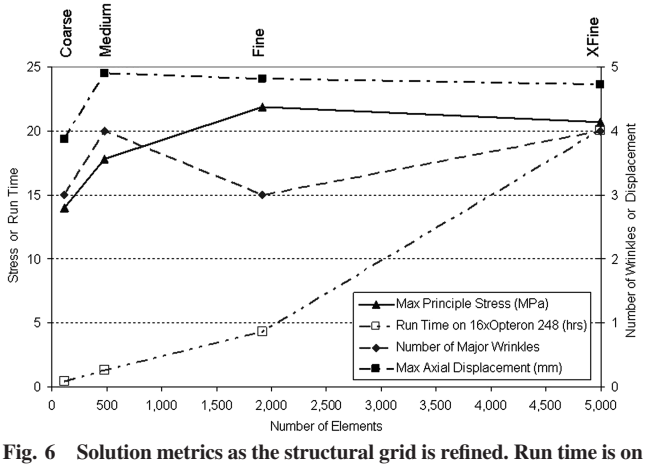

Fig. 6 Solution metrics as the structural grid is refined. Run time is on 16 Opteron 248 processors.

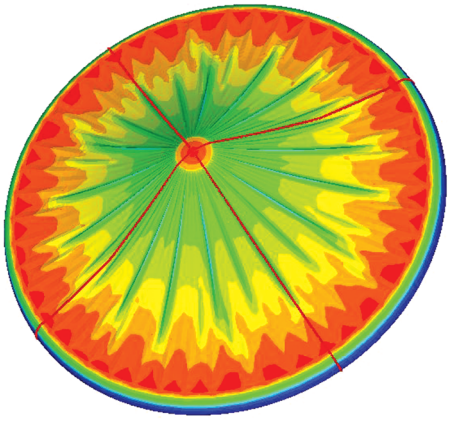

Fig. 7 Static coupled solution, with low-fidelity aerodynamics, of the ISP wind-tunnel model with surface pressure contours. Red indicates higher pressure, more blunt surfaces, and the dark red lines are reflection boundaries.

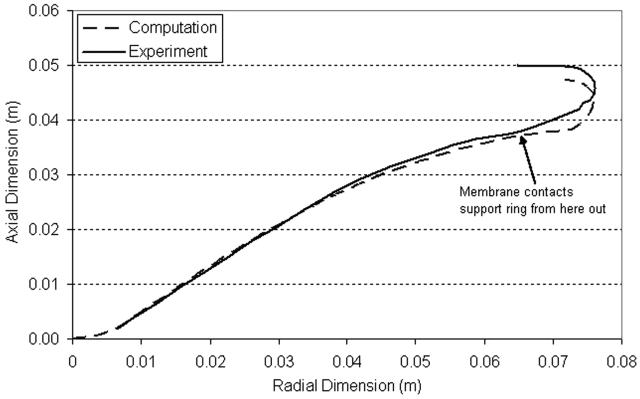

Fig. 8 Radial profile of the static coupled solution of the ISP wind tunnel model.

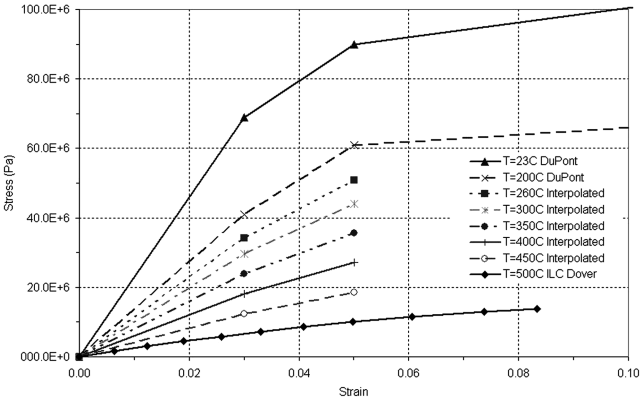

Fig. 9 Kapton 30HN stress–strain relation at various temperatures.

these two cases. The addition of thermal expansion causes the support ring to move aft, but not quite as far as the experiment. Even without thermal expansion, increasing the temperature to 350°C allows the support ring to move aft, but not as much as the addition of thermal expansion. From these two results it appears that some combination of thermal expansion and increased temperature will result in a nearly perfect match to experiment. Unfortunately, due to the interference of the aft support ring at a radius of approximately 0.065 m in the test, the computation will not precisely match the experiment in this region (because the computational model does not include contact and the internal support structure geometry is not known).

Trial and error was used to determine the proper temperature required to match the experimental data. Figure 11 shows the profile with the best fit, which includes thermal expansion at a temperature of 300°C. Increasing the temperature beyond 300°C did not increase

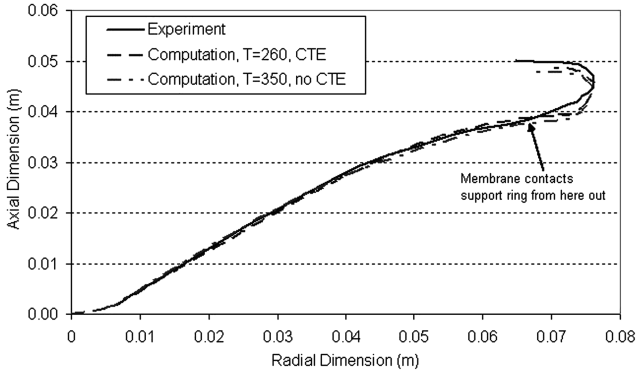

Fig. 10 Radial profile with $T = 350°C$, and $T = 260°C$ with thermal expansion. CTE = coefficient of thermal expansion.

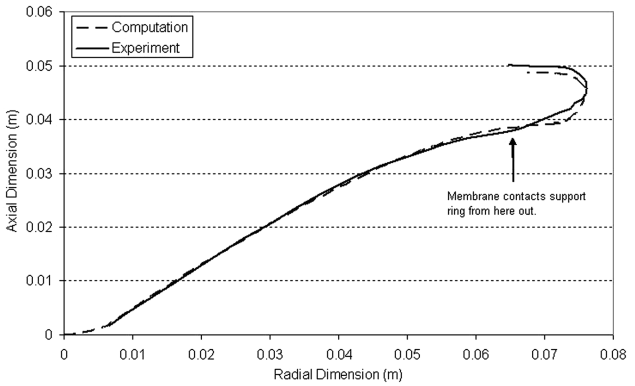

Fig. 11 The best computational solution includes thermal expansion at 300°C.

the deflection of the aft ring, but instead caused excessive deflection of the membrane.

D. Coupled High-Fidelity Aerodynamic Solution

High-fidelity analysis was performed by coupling NASCART-GT to LS-DYNA. Preliminary grid studies were performed with NASCART-GT to determine the necessary grid resolution, and coupled analysis was run with the best grid resolution for both NASCART-GT and LS-DYNA.

1. NASCART-GT Grid Convergence Study

Grid studies in NASCART-GT were performed using the deformed geometry from the wind-tunnel tests. The profile used was taken from the photograph used for shock structure comparison in the left half of Fig. 12, and a three-dimensional grid was generated by sweeping the experimentally determined deformed profile 90° to form a solid body. This approach generates an average deformed surface because it does not contain the surface wrinkle patterns. The number of cells used to define the body in NASCART-GT was then varied and the axial force coefficient (C_z) was used to judge convergence. Four of the grids used in the study are shown in Fig. 13 with Mach number contours of the flowfield. The shock structure is nearly identical in all of the grids studied, and Fig. 12 compares the shock structure computed with NASCART-GT using the M3 grid and a photograph from the wind-tunnel test. The shock structure in the photograph was enhanced by applying a different color map to the image and adjusting the contrast. Good agreement is observed between the computed and experimental shock structures.

Figure 14 shows the axial force coefficient for each grid used in the grid study. The grid with approximately 200,000 cells on the surface (M3 grid) appears converged, but during coupled analysis it was discovered that NASCART-GT had difficulty with the surface boundary conditions over the fine wrinkles at this grid density. Better results were obtained using the F1 grid (approximately 380,000 cells on the surface) so this grid will be used for the subsequent coupled analysis.

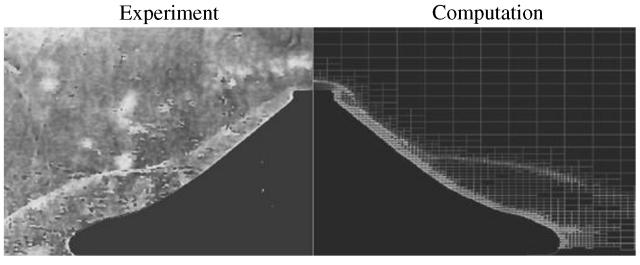

Fig. 12 The computational solution shows good agreement with the experimentally observed shock structure.

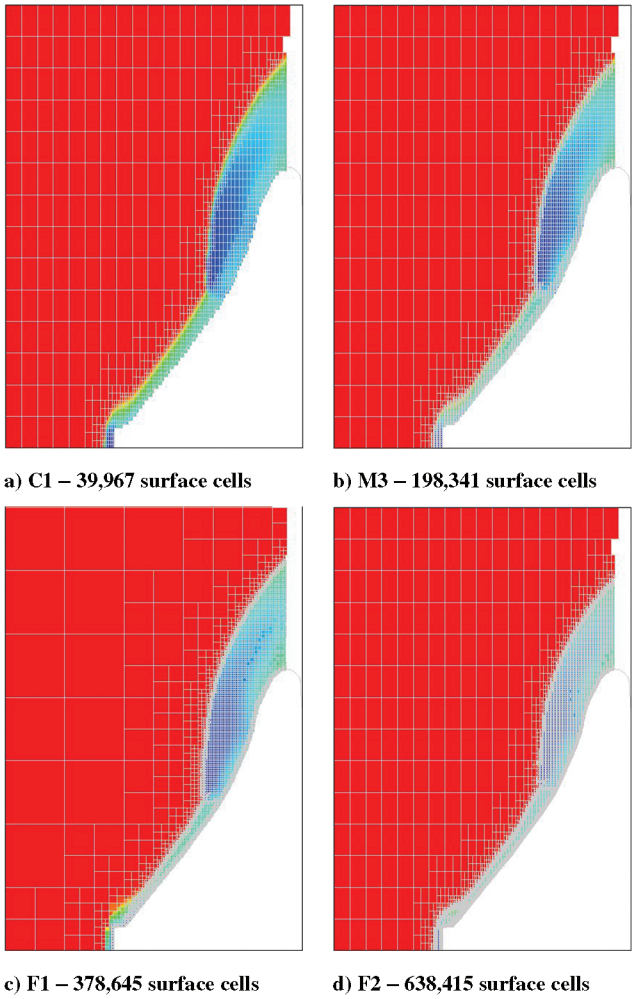

Fig. 13 Grids used in the NASCART-GT convergence study of the ISP wind-tunnel test model. Red indicates higher Mach number.

2. High-Fidelity Coupled Results

The coupled analysis was initiated using modified Newtonian analysis for the first iteration and NASCART-GT for subsequent iterations. In the high-fidelity analysis, the structural model was run for 2.5 s between each iteration with artificial damping applied to allow vibrations to damp out between CFD analyses. These two enhancements were made in an effort to save computation time because only a static deformed shape is desired and the CFD analysis takes approximately 4 times longer than the structural analysis.

For each coupling iteration, NASCART-GT required approximately 5000 iterations to converge. Figure 15 shows the axial force coefficient and the numerical residual both reaching constant values,

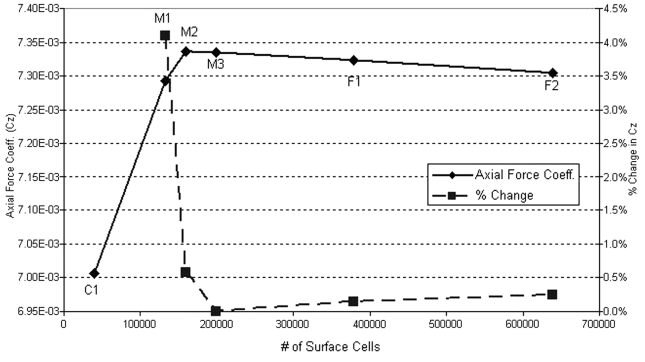

Fig. 14 NASCART-GT grid convergence study showing good convergence for all models with 200,000 surface cells or more. Here the axial force coefficient is calculated using a reference area of 1.0 m^2.

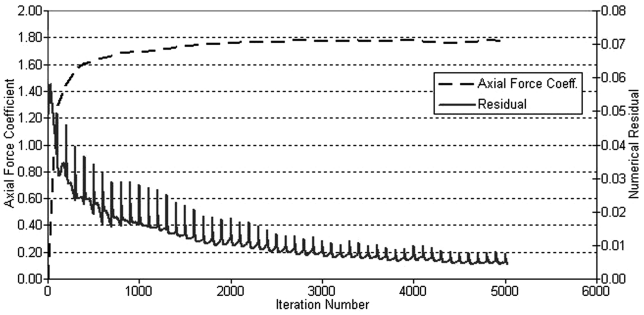

Fig. 15 NASCART-GT convergence of numerical residual and axial load coefficient for coupled iteration 6.

demonstrating that 5000 iterations are sufficient to converge the pressure loads.

The coupled solution was run for six iterations at which point the last three iterations had changed the axial deformation less than 0.1% as shown in Fig. 16. The resulting profile of the deformed shape is shown in Fig. 17. This deformation is very close to that obtained using the low-fidelity aerodynamic analysis (Sec. III.C). The high-fidelity solution surface pressure distribution and flowfield Mach number are shown in Fig. 18. The discontinuous high pressure ring on the surface is due to shock–shock interaction and is disturbed where surface wrinkles pass through the interaction region. The flowfield shows a very similar structure to that obtained in the experiment (Fig. 12), though the deformed shape near the outer radius of the model is slightly different and causes the shock to be less curved.

E. Comparison of Low- and High-Fidelity Validation Results

When NASCART-GT pressure data are used in the coupled analysis, the results are essentially the same as for the modified Newtonian analysis (Figs. 7 and 18). The primary differences are that NASCART-GT predicts constant pressure over the wrinkles, and a

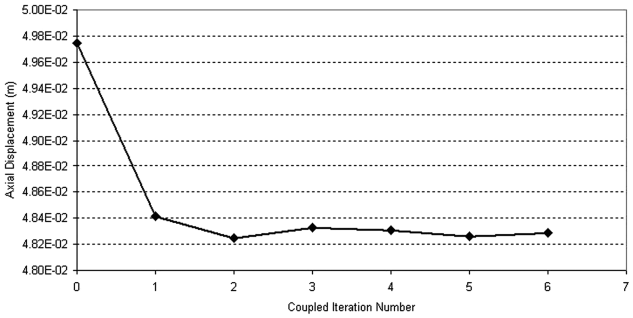

Fig. 16 Convergence of axial displacement of the ISP wind-tunnel validation case.

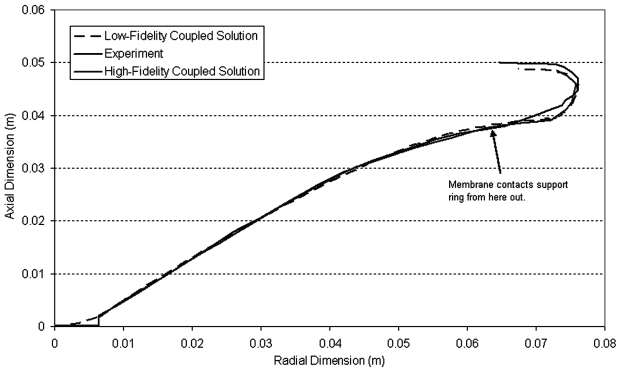

Fig. 17 Deformed profiles from NASCART-GT and modified Newtonian aerodynamics compare well with experiment.

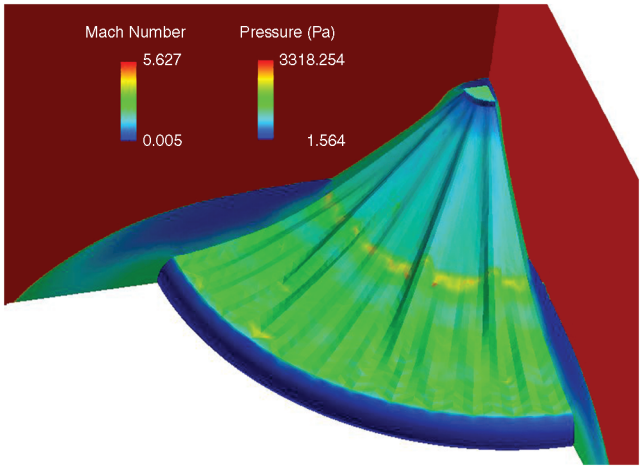

Fig. 18 Surface pressures and flowfield Mach number distribution computed by NASCART-GT on the deformed geometry.

high pressure region due to shock–shock interaction at about two-thirds the vehicle radius. Figure 19 illustrates the differences in surface pressure between CFD and modified Newtonian aerodynamics. Despite the difference in pressure distribution, the deformed profiles are nearly identical, indicating that the deformed shape of this geometry is relatively insensitive to pressure distribution.

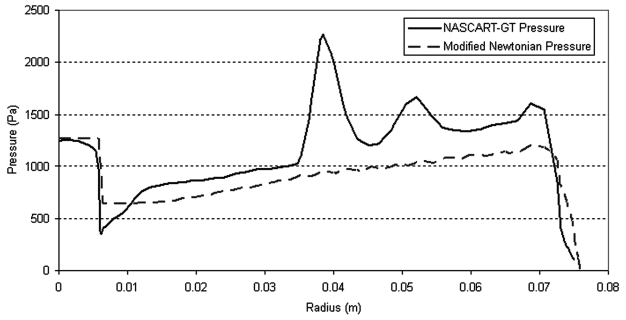

Fig. 19 Surface pressure variation with radius for both NASCART-GT and modified Newtonian aerodynamics. The pressure spike at 0.4 m radius is due to shock–shock interaction.

Furthermore, the stress distribution in the membrane is nearly identical for both low- and high-fidelity models. Figure 20 shows the stress distribution in both models and indicates that the peak stress in the high-fidelity model is 27% higher, even though the peak stress is at the nose attachment point in both models. This is in-line with the 25.6% higher drag predicted by the high-fidelity aerodynamics, because the material area and wrinkle patterns are the same in both cases. The nearly identical deformed shapes, despite the differences in drag and stress, are attributed to the Kapton membrane being thick and stiff relative to the model size.

Profiles from both low- and high-fidelity models match experiment very well considering the orientation of the profile in the test data is unknown relative to the surface wrinkling, no quantifiable data were obtained during the test itself, and the membrane contact with the aft support ring is unmodeled. Three-dimensional surface contours from test data could remedy this problem, but are currently unavailable.

IV. Ballute Static Aeroelastic Analysis

Aerocapture is possible at any body with a substantial atmosphere and is of particular interest for missions to the outer planets. Titan, in particular, has been studied extensively as a target for an aerocapture mission. The mission selected as the example problem has been documented extensively in Miller et al. [18,24], Johnson and Lyons [25], Westhelle and Masciarelli [26], Brown and Richardson [27], and James et al. [28].

A. Ballute Trajectory

The trajectory used in this study was computed for a 1000-kg spacecraft inserting into a 1000-km circular orbit about Titan with an atmospheric entry velocity of 6.5 km/s (atmospheric interface at 1000 km). The aerodynamic drag used in the trajectory analysis assumes a rigid clamped ballute with a 12.1-m major radius, a 1.73-m minor radius, and a 60-deg cone half-angle.

The trajectory is bounded on the steep side by a heat rate limit of 3 W/cm^2 and on the shallow limit by the minimum velocity change required to insert into a 1000-km altitude circular orbit. Aeroelastic solutions will be calculated at two points on the steep aerocapture trajectory because the steep trajectory produces the highest aerodynamic loads. The peak dynamic pressure point will be analyzed because it is the highest loading on the trajectory, and a point in the transitional regime will be analyzed. The two conditions chosen are listed in Table 3. All aerodynamic analysis presented assumes a perfect gas with a constant ratio of specific heats.

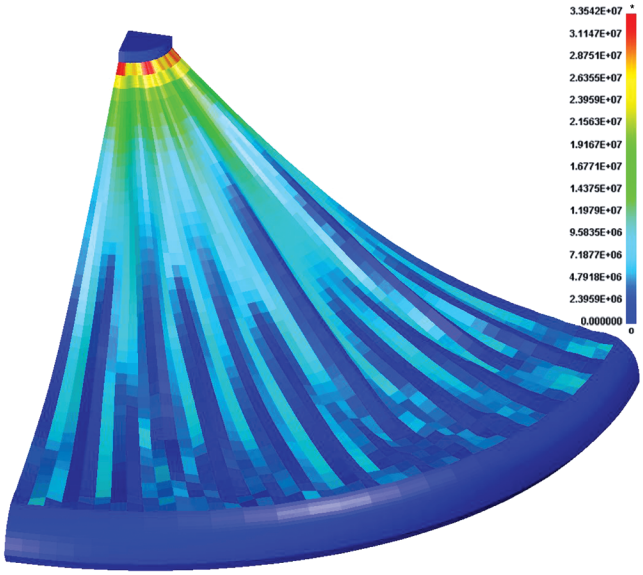

a) High-fidelity stress distribution

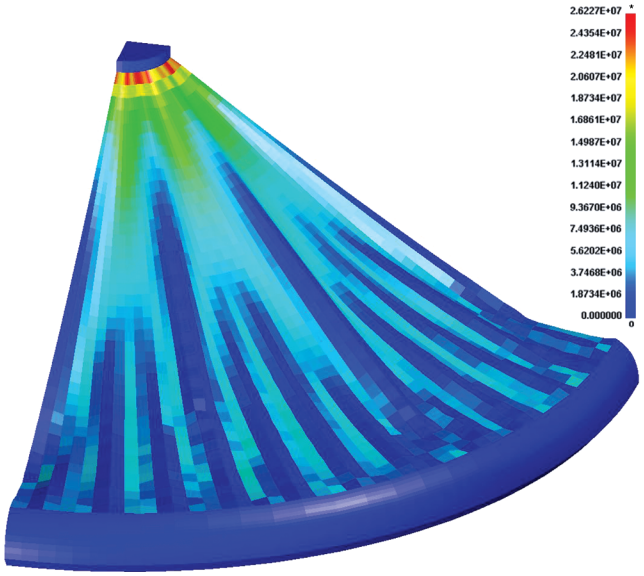

b) Low-fidelity stress distribution

Fig. 20 Stress distribution in the ISP wind-tunnel model for both low- and high-fidelity solutions (Principal-1 stress in Pa).

Table 3 Trajectory data for two points on a Titan aerocapture trajectory

Parameter	Peak dyn. press. point	Transitional point
Velocity, m/s	4266.4	6512.0
Atm. density, kg/m^3	5.66×10^{-6}	2.05×10^{-8}
Atm. temperature, K	166	202
Atm. pressure, Pa	1.22×10^{-3}	2.73×10^{-1}
γ	1.424	1.416
Gas constant, J/kg · K	286.9	288.6
Knudsen no.	0.002	1.0
N_2 mole fraction	89.71%	92.04%
CH_4 mole fraction	1.09%	1.98%
Ar mole fraction	9.20%	5.98%

B. Ballute Geometry

The configuration selected for analysis is shown in Fig. 21. Structural analysis of this configuration revealed too high a stress level near the ballute-to-spacecraft attach point to use a polymer membrane for the entire cone so a 3.556×10^{-4}-m thick Nextel fabric is used for the inner 6.1 m of the cone. The remainder of the ballute is constructed of Upilex of 5.08×10^{-5}-m thickness in the cone, and 3.4×10^{-4}-m thickness in the torus. Torus thickness was determined using FEA, and fill pressure was chosen to avoid buckling, resulting in a fill pressure of 2000 Pa.

1. *Ballute Material Properties*

The properties of Upilex are affected by temperature, and this is accounted for in the structural model. Unfortunately, ballute temperature is only known at the peak dynamic pressure point and is applied to the ballute as a uniform temperature of 228°C. For the transitional point the temperature is unknown and so is estimated at 100°C for the purpose of this study. The temperature data are applied to the material properties, producing a lower modulus material. Thermal expansion was not included in these models because it produced a numerical instability for which a solution has not been found. More work is necessary in the area of thermal modeling to determine the actual ballute temperature, to model variable temperature material properties, and to include thermal expansion effects.

The properties of Upilex SN are listed in Table 4 at the two temperatures used. The modulus and Poisson ratio of Nextel 312 AF-10 fabric are essentially constant at 7 GPa and 0.20 over the temperature range from 0 to 400°C, while the yield stress drops from 118 to 88 MPa over the same temperature range [29].

2. *Ballute Structural Grid Convergence*

The ballute was modeled in LS-DYNA as a quarter model using quadrilateral shell elements. A grid convergence study was performed with this model using a fixed aerodynamic load based on the initial geometry and using between 12,736 and 450,560 elements. Aerodynamic loading is calculated using the modified Newtonian method for speed, and a sample of the grids used in the study is shown in Fig. 22. Convergence of the structural model was based on axial displacement and von Mises stress because displacement determines the aerodynamic loading and von Mises stress is a good measure of failure for isotropic materials. Figure 23 shows that the model with 348,705 elements was adequately refined and will be used for the remainder of this study.

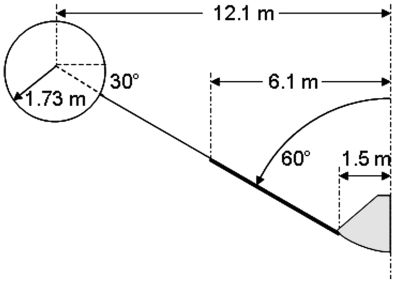

Fig. 21 Clamped ballute configuration used for Titan aerocapture.

C. Results Using Low-Fidelity Aerodynamics

The two trajectory points listed in Table 3 were both run using the low-fidelity aerodynamics tools to estimate the deformation. A low-fidelity structural grid (the Fine3 model with 111,240 elements) will also be used with this analysis to reduce computation time because the intent of the low-fidelity tool is to provide a rapid design tool. This introduces a 15% difference in displacement compared to the high-fidelity model. Both points fall in the transitional regime as defined in Table 1 and will use the bridging function to compute surface pressures.

1. *Peak Dynamic Pressure Point Analysis*

The peak dynamic pressure case is nearly in the continuum regime and primarily derives surface pressure from the modified Newtonian analysis. The resulting axial displacement of the torus is 0.13 m in the flow direction and the maximum von Mises stress is 37.1 MPa, well below the yield stress. The deformed shape with surface pressure contours is presented in Fig. 24 and shows clearly defined surface wrinkles.

2. *Transitional Results*

The transitional regime case is nearly in the rarefied regime and is mostly influenced by the collisionless DSMC calculation. Because of the substantially lower atmospheric density, the axial deflection of the torus is −0.7 m (moving forward) and the maximum von Mises stress is 22.5 MPa. The deformed shape with surface pressure contours is shown in Fig. 25. At this flight condition the pressure is not high enough to stretch the conic membrane taught, and the wrinkles that have formed are not fully stretched, as seen in the peak dynamic pressure analysis. The wrinkles that have formed in the membrane wander on the surface and have secondary kinks in their structure, causing locally high stresses despite the relatively low drag load. The edge where the fabric and polymer membrane join is visible as the smaller diameter ring of lower pressure at the middle of the cone since the deflection there changes due to the changing material properties.

D. Results Using High-Fidelity Aerodynamics

The same two trajectory points used in the above low-fidelity analysis were run using the high-fidelity aerodynamics tools to determine a more accurate deformation. A high-fidelity structural grid (the Fine6 model with 348,705 elements) will be used with this analysis.

1. *Continuum Analysis at the Peak Dynamic Pressure Point*

The peak dynamic pressure point has a Knudsen number of 0.002, which is just outside the continuum range according to the analysis of Sec. II.B, but in the area of overlap between CFD and DSMC analyses. Because of the relativiely high density at this point, DSMC analysis is computationally too expensive, so NASCART-GT will be used.

a. Grid Convergence in NASCART-GT. To verify that the grid resolution was not affecting the results from NASCART-GT, a convergence study was performed using the undeformed clamped ballute geometry. The parameter *nbmin* was varied from 32 up to 128 to increase the grid density. Drag is used as the convergence

Table 4 Material properties of Upilex

Material property	100°C	228°C
E, GPa	4.692	3.883
ν	0.34	0.34
Yield stress, MPa	210.0	130.0

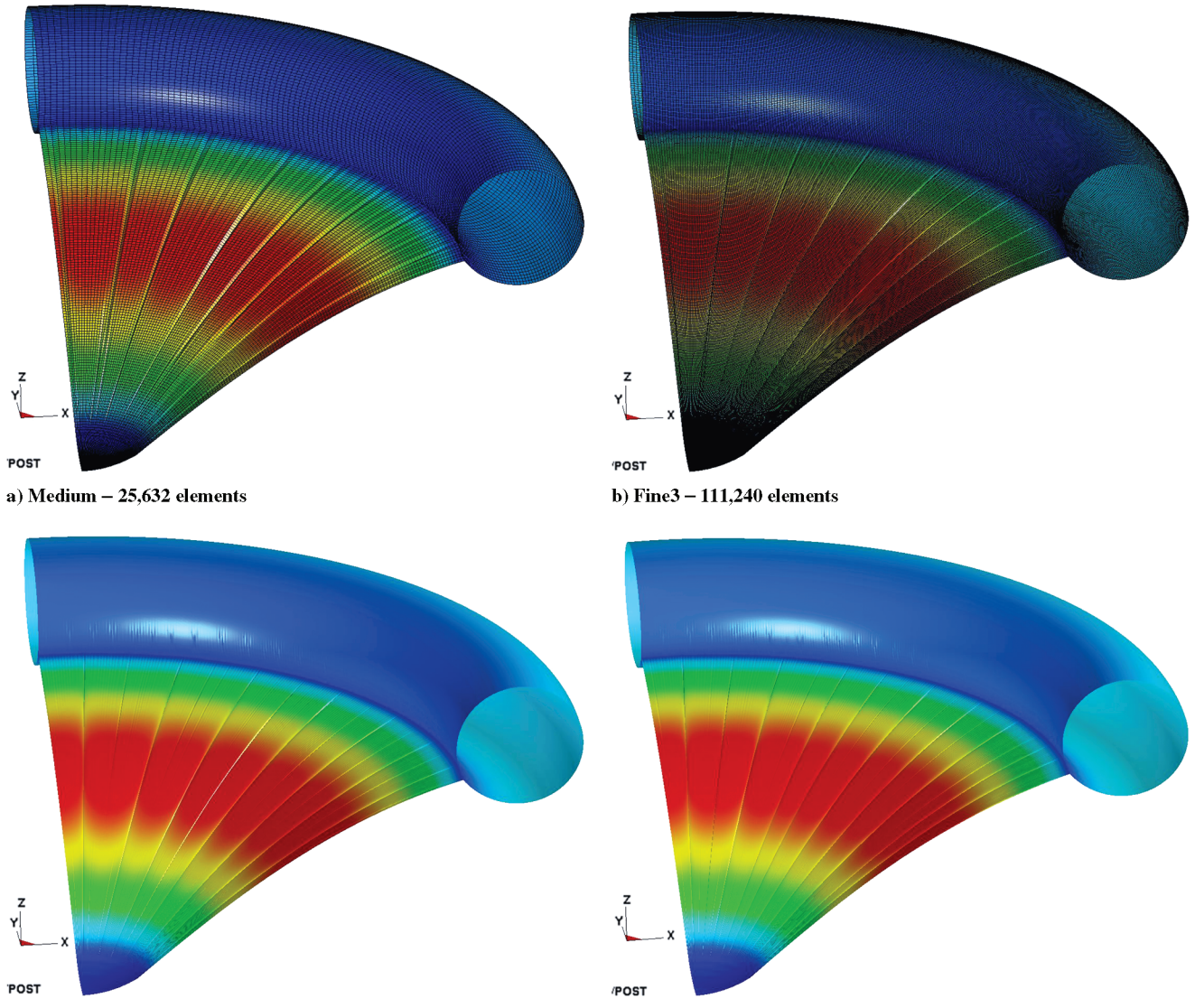

Fig. 22 Grids used in the clamped ballute convergence study. Element edges are not shown for the Fine grids since the model would appear black. Red indicates larger axial displacement.

metric because it is a significant contributor to the deformation of the structure. Figure 26 shows the drag as the grid density is varied. The change in drag between the grids with $nbmin = 64$ and $nbmin = 128$ is less than 1%. The surface pressure distributions for the grids with $nbmin = 64$ and 128 are shown in Fig. 27, and it is apparent that the grid resolution causes a decreased pressure at the attachment of the cone and torus near the symmetry plane for the coarser model. For

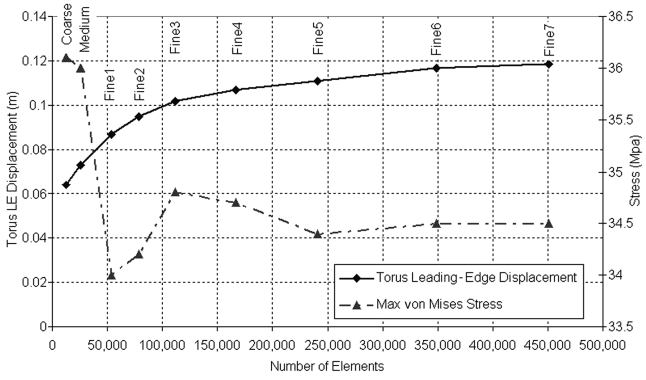

Fig. 23 Grid metrics used to determine convergence of the clamped ballute structure model.

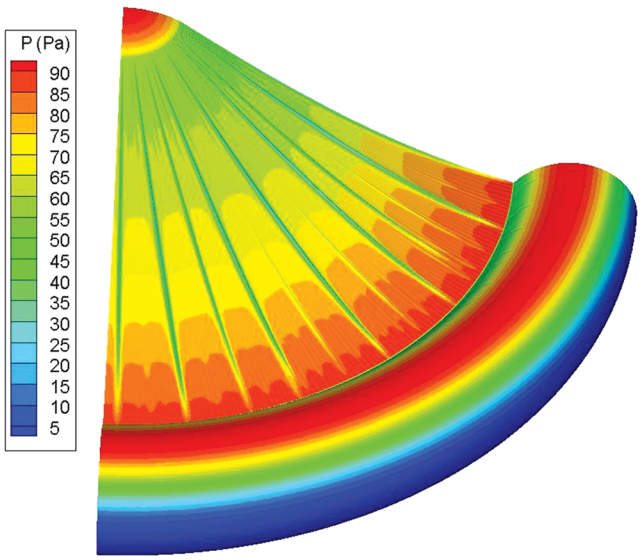

Fig. 24 Deformed clamped ballute at peak dynamic pressure with surface pressure contours in Pa.

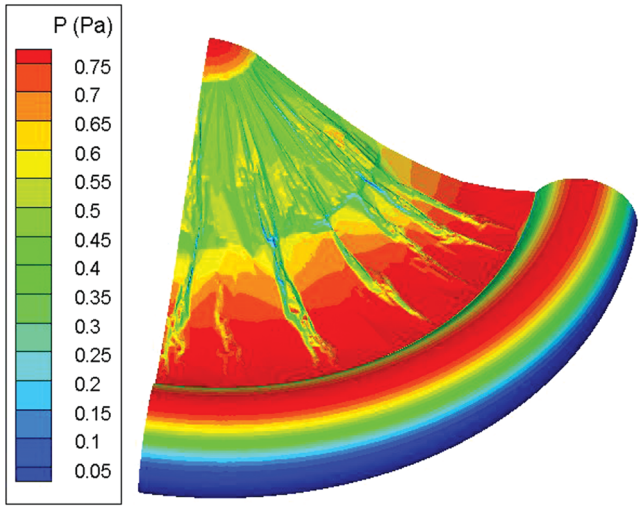

Fig. 25 Deformed clamped ballute in transitional regime with surface pressure contours.

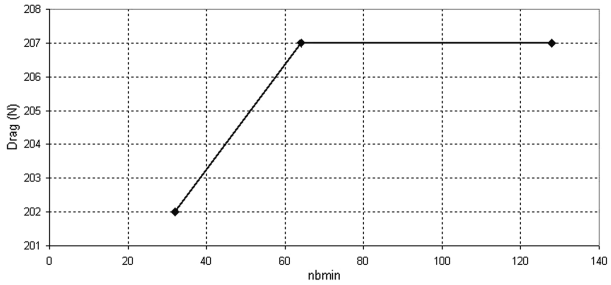

Fig. 26 Computed drag force indicates that grids with *nbmin* greater than or equal to 64 are grid independent.

this reason, the grid with $nbmin = 128$ (Fig. 28) will be used for the coupled analysis presented in the following section.

b. Results of Continuum Analysis at the Peak Dynamic Pressure Point. A coupled case using a quarter model was run using NASCART-GT and the Fine6 structural model and the $nbmin = 128$ aerodynamic grid. Because of the computational grid generation process in NASCART-GT, the structural grid is coarsened for input to NASCART-GT. The surface input grid to NASCART-GT shares every fifth node in the radial and circumferential directions with the structural model so that no interpolation is required for displacement transfer. The pressure mapping process is described in detail in Sec. II.C. Grid coarsening causes the surface wrinkles to be smeared, but the NASCART-GT Cartesian grid does not fully capture them, so no resolution is lost. Figure 29 shows the structural grid, the NASCART-GT input grid, and the NASCART-GT computational grid from the last coupling iteration.

The solution took five iterations to converge (Fig. 30), and 5 days of computer time when running NASCART-GT on 21 processors (15 AMD Opteron 248 and 6 AMD Opteron 280) and LS-DYNA on 31 processors (15 AMD Opteron 248 and 16 AMD Opteron 280). The resulting deformed shape with surface pressure and freestream Mach number is shown in Fig. 31. Close inspection of the pressure on the deformed body indicates some pressure variation along the two symmetry planes. A full three-dimensional model was run, and it was determined that the pressure variations are due to the symmetry conditions since they do not exist in the full model. The pressure variation is limited to within two aerodynamic computational cells of the boundary and is less than 5% different than pressures in the full model. Because of the small variation and proximity to the boundary, these variations will be neglected, and no data along either symmetry plane will be used.

The deformation results in a peak von Mises stress of 38.9 MPa and a peak principal stress of 41.1 MPa, both which occur in the membrane where it attaches to the fabric inner cone. Figure 32 shows the von Mises stresses of the deformed configuration, with the rigid spacecraft in dark blue.

2. *Transitional Regime Analysis*

The transitional case was run using the DAC software as a point of comparison for the low-fidelity aerodynamics tool.

a. DSMC Grid Study. DAC uses a Cartesian grid which affects the execution time and accuracy of results. A trade-off can be made between the number of iterations to run and the number of real-to-simulated (RTS) molecules. The primary constraint on the

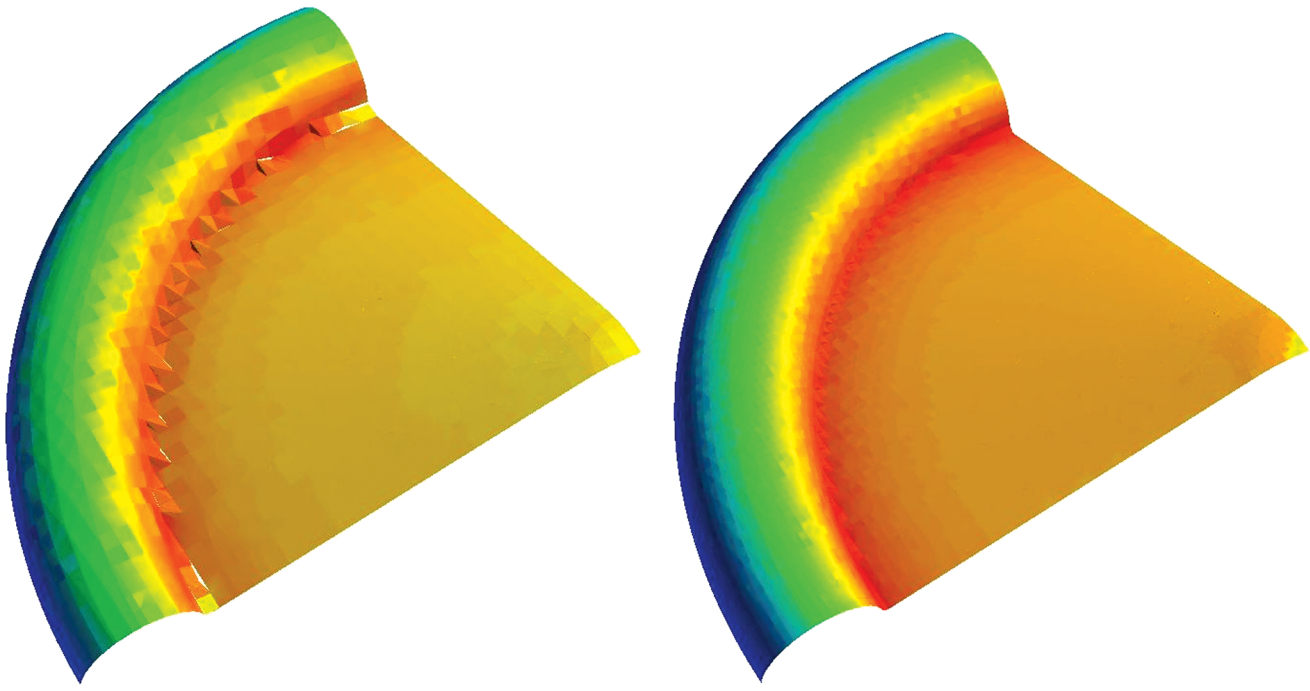

a) *nbmin* = 64 **b) *nbmin* = 128**

Fig. 27 Surface grids computed by NASCART-GT. The coarser grid does not properly capture the inside corner and underpredicts pressure near the symmetry plane. Red indicates higher surface pressure.

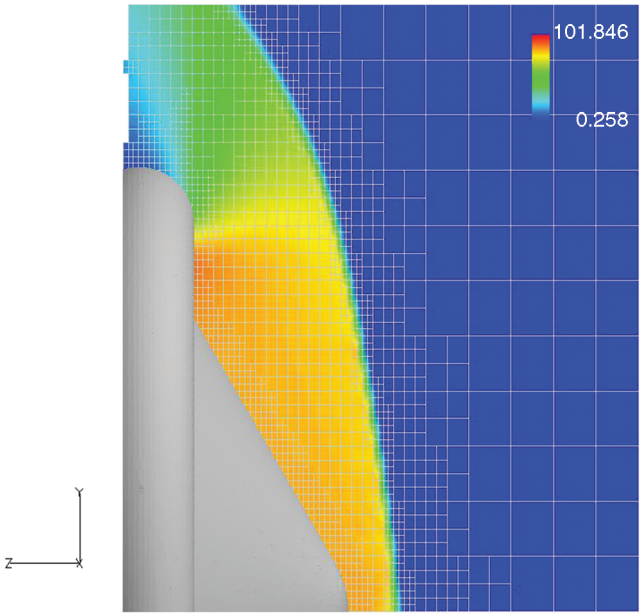

Fig. 28 Pressure countours (in Pa) around the undeformed clamped ballute model with *nbmin* = 128.

grid is to have cells smaller than 1 local mean-free path (λ) so that collisions occur between molecules within reasonable spatial proximity. DAC can adapt the grid to meet the local λ requirement on cell size, but the process requires manual input and would require substantial work to automate. The primary goal of the grid study is to find the fastest combination of grid size and RTS molecule ratio that produces good force output and does not require adaptation. Furthermore, the dimensions of the simulated domain have an affect on the solution, and this will be studied using the best grid size and RTS molecule count.

For this flight condition the freestream λ is approximately 25 m. This study looks at grids with cell dimensions ranging from 1 m down to 0.12 m in four steps, and with RTS molecules ranging from 1×10^{18} to 1×10^{14}. Figure 33 shows a slice through the flowfield for each grid used in the study and the flowfield temperature using 1×10^{14} RTS molecules. The back of the body was closed off to produce a solid geometry for automatic mesh generation and because the flow in the wake does not affect the pressure on the forebody. The grid size is overlaid on the flowfield temperature results because DAC produces a different grid for results output than is used for the computation. All simulations assume a noncatalytic wall with diffuse particle interaction and only translational and vibrational modes of the gas are considered.

Each grid test was run until the forces converged, and the execution time required to reach a converged solution is shown in Table 5 along with the resulting axial force. For each grid and RTS molecule count, the solution was considered converged when the change in the forces or moments was less than 0.1% for at least three consecutive output intervals. The coarse grid did not converge in 5 times the number of iterations required to obtain a converged solution in the other three grids, so adaptation was performed in an attempt to obtain a solution. The adapted grid produced the same forces and moments as the other three grids, but required substantially more time and grid adaptation, ruling it out for use in coupled solutions. As the RTS molecule count increased (fewer simulated molecules) the resulting axial force started to vary. The Medium, Fine, and XFine grids all produced the same axial force without grid adaptation (using 1×10^{14} RTS molecules), but the time required was minimum for the Medium grid. Because the time required for the Medium and Fine grids with 1×10^{16} and 1×10^{15} RTS molecules, respectively, is very small compared to the time to

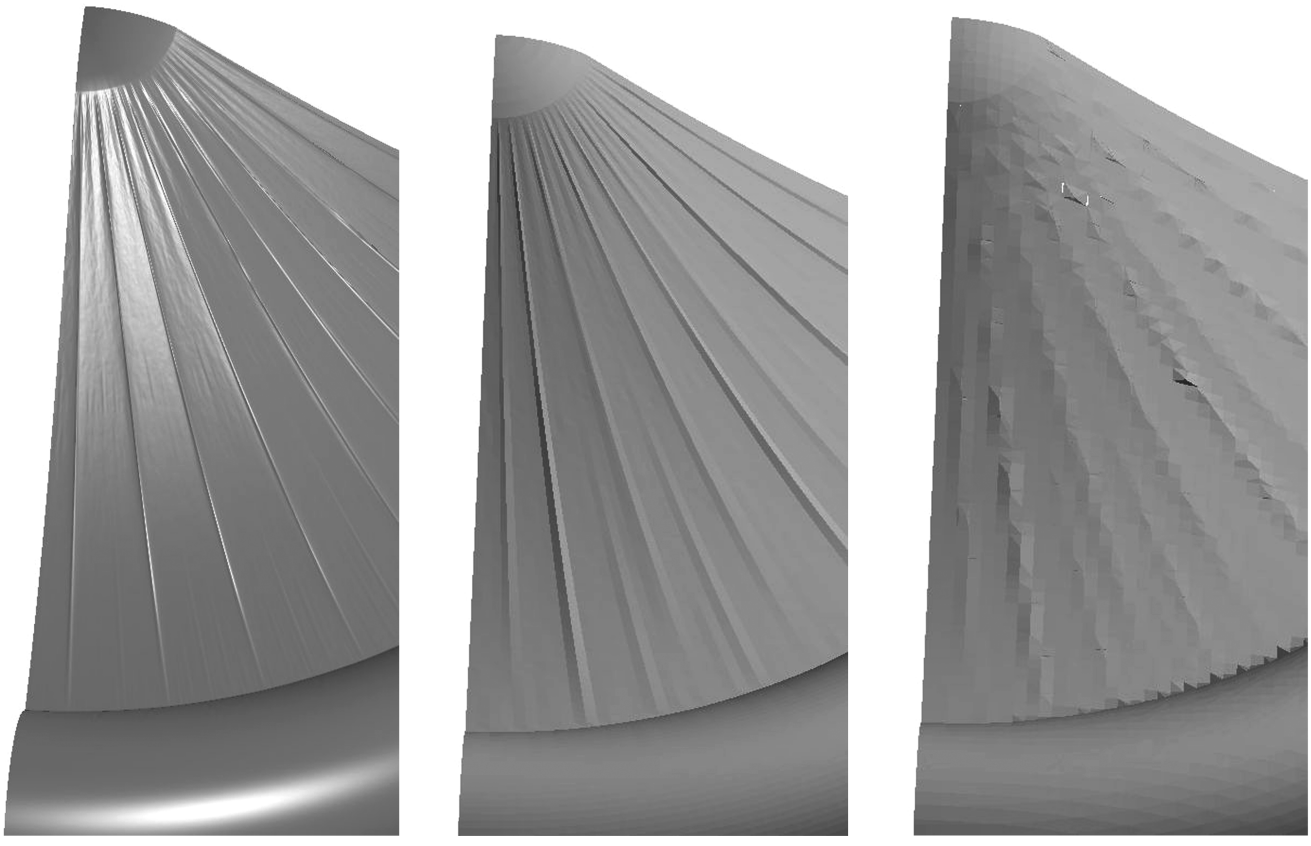

a) Structural grid **b) CFD input grid** **c) CFD computational grid**

Fig. 29 Comparison of the three surface grids used in high-fidelity coupled analysis with NASCART-GT shows that no detail is lost by coarsening the input grid.

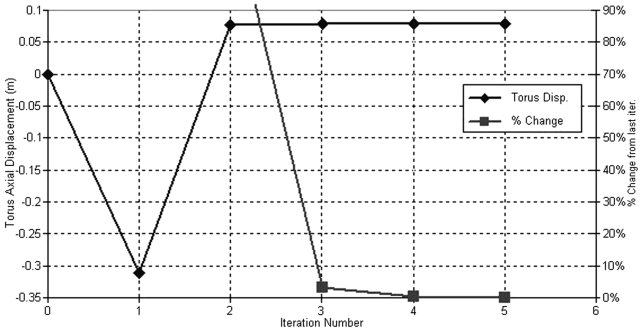

Fig. 30 Convergence of the high-fidelity coupled solution using NASCART-GT.

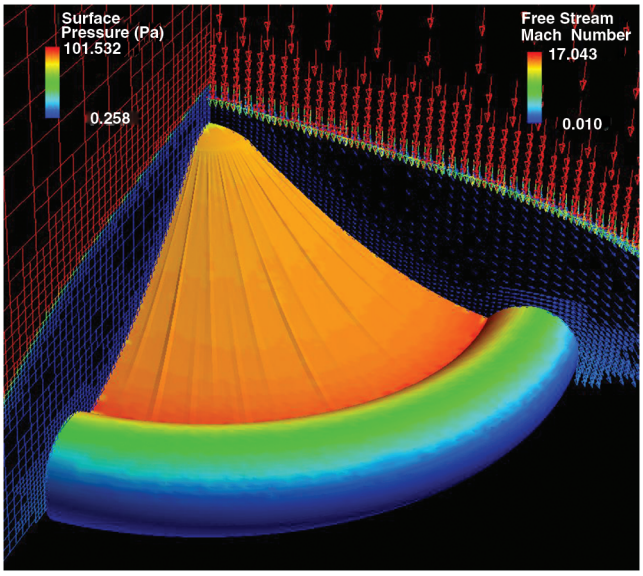

Fig. 31 Surface pressure countours and freestream Mach number around the deformed ballute, showing the input surface grid.

run the structural model, the Fine grid was chosen because it can resolve the surface wrinkles more accurately. The Fine grid with 1×10^{15} RTS molecules will be used to study the domain size and for coupled solutions.

Because the front of the shock is not quite included in the domain used for the grid study, the domain size was explored. Domain dimensions and axial force are listed in Table 6 along with the relative change in axial force. The Fine grid pictured in Fig. 33c is domain size 2 in this study, with one smaller domain and six larger domains explored. Domain size 8 increases the width over domain size 7 and shows that further increases in the width of the domain do not affect the solution. Domain size 6 appears to have reached a converged axial force with a relative change in force of less than 1.0% and will be used for the coupled solution. Figure 34 shows the flowfield temperature of domain size 6 and the thicker shock compared to Fig. 33c.

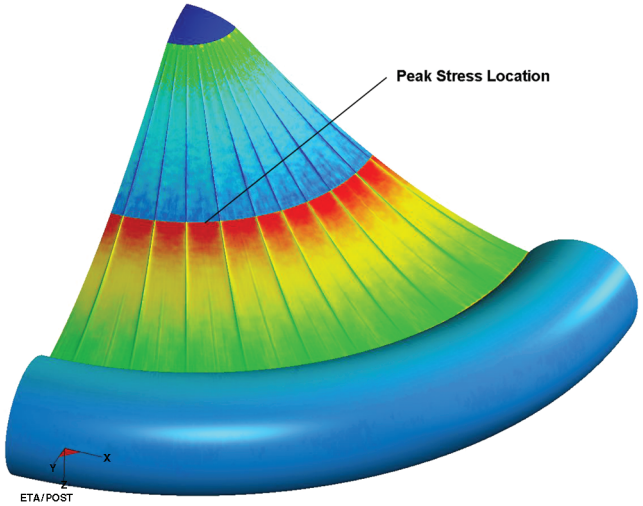

Fig. 32 Peak von Mises stress occurs at the seam between fabric and membrane on the deformed clamped ballute. Red indicates higher stress.

b. Transitional Results. A static coupled solution was computed for a quarter model of the clamped ballute using the Fine6 structural grid and the Fine aerodynamic grid with domain size 6. A quarter model was chosen because off-axis deformations are not expected and surface wrinkles can still be captured. The model includes a backface to close the body (as seen in Fig. 33) for aerodynamic analysis which is not included in the structural analysis. Elements on the torus which are internal to this structure have no aerodynamic pressure applied to them because they are in the wake where the pressure is very low.

The structural analysis was run for 30 s between each coupling to allow the solution to damp out any oscillations between aerodynamic analyses. Because the above grid study was performed on an undeformed geometry, the aerodynamic analysis was run for 4000 iterations to leave a sufficient buffer such that the solution is statistically significant even if it takes longer than for the undeformed shape. Figure 35 shows the forces from the DAC model converging (at iteration 1000) well before the run completes on the final coupling iteration. The resulting deformation is shown in Fig. 36 with surface pressure contours on the body and temperature contours on the flowfield slice. The convergence history of the axial displacement of a node on the leading edge of the torus is shown in Fig. 37. The drag on the deformed body is 118.7 N, well within 1% of the undeformed body, indicating that coupled analysis is not necessary in the upper end of the transitional regime to get accurate drag predictions for performance analysis. This should be expected because the deformation is much smaller than the shock standoff distance and, as such, will not have much affect on the flowfield.

E. Comparison of Low- and High-Fidelity Ballute Results

At the peak dynamic pressure point there is good agreement between the low- and high-fidelity solutions for stress and drag, as seen in Table 7. Peak stresses occur in the same location (at the joint between fabric and membrane) in both models. The axial deflection of the torus is significantly different despite the small difference in overall drag, which is due to the difference in pressure distribution.

There are two key differences in the pressure distribution between the low- and high-fidelity models. In the high-fidelity model there is a detached shock wave that encompasses the entire body, and a pocket of high pressure at the torus/membrane attachment. The low-fidelity model lacks this high pressure region, but instead predicts approximately 50% higher pressure on the front face of the torus. This difference in pressure distribution accounts for the 8% difference in total drag on the quarter model and the difference in the axial displacement of the torus.

At the transitional regime point on the trajectory, analysis was performed using both low-fidelity impact methods and DSMC aerodynamics. Several significant differences are observed including the torus axial deflection and the peak von Mises and principal stress in the membrane (Table 8).

The difference in torus axial deflection is caused by the pocket of high pressure at the junction of the conic membrane and torus in the DSMC calculations. This produces a moment that rolls the torus outward compared to the low-fidelity analysis.

The difference in the peak von Mises stress is due to slight differences in the wrinkle formation, which is influenced by the local surface pressure around the wrinkles. Figure 38 shows a close-up of the peak stress location and the difference in wrinkle shape for both low- and high-fidelity models. In the low-fidelity analysis, the pressure on the wrinkles is substantially lower than the surrounding areas, which allows the wrinkles to be less well defined. In the DSMC

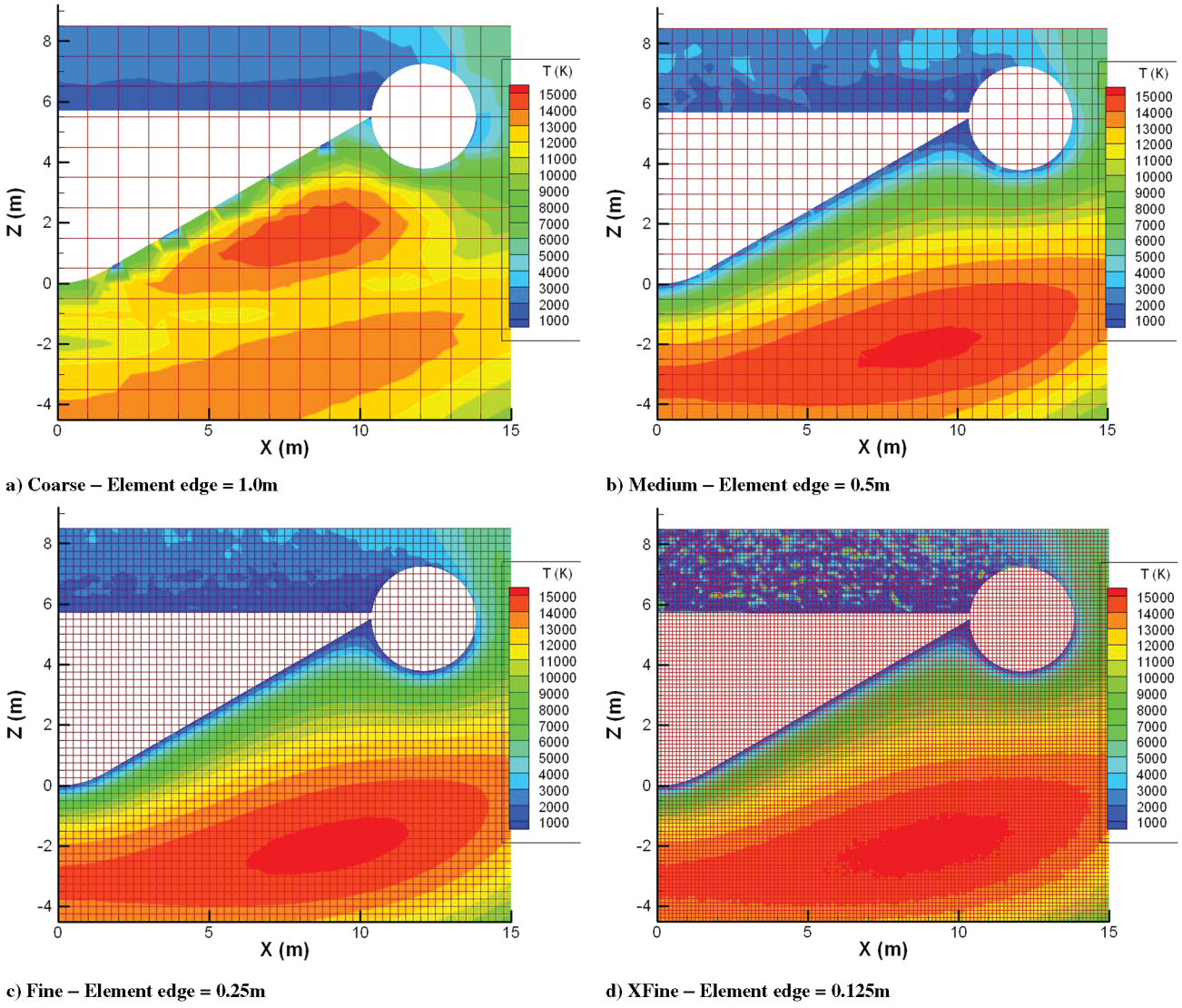

Fig. 33 The grids used in the DAC grid convergence study.

results, the pressure is much closer to the surrounding area over the wrinkles, forcing them to become better defined and much narrower. Because of the lower pressure, the wrinkles in the low-fidelity analysis have kinks in them which produce locally high stress levels. Furthermore, the peak stresses in the low-fidelity model occur at bends with small radii, and the element formulation used does not support bending, nor does it have sufficient resolution to properly capture such small radii. In addition, this point on the trajectory provides insufficient drag to fully stretch the ballute.

The predicted drag is 13% lower in the DSMC analysis which is probably sufficient for conceptual design considering the low total drag. The difference is likely due to the low-fidelity aerodynamics computing low pressure at the joint between the torus and membrane, whereas the DSMC analysis predicts high pressure in that region. This causes the lower integrated drag on the low-fidelity model and a different loading, with the high-fidelity model being stretched more radially than the low-fidelity model, contributing to the better formed wrinkles in the high-fidelity model.

Table 5 Time to converge each run (min) and axial force (N) in the DAC grid convergence study. Bold indicates the fastest run times with good drag values, and italic indicates runs with poorly predicted drag

RTS Molecules	Medium	Fine	XFine
1×10^{14}	41/126.9	36/126.8	39/126.6
1×10^{15}	4.5/126.9	**3.1/126.5**	21/126.1
1×10^{16}	**1.3/126.5**	*1.1/125.6*	*3.3/125.2*
1×10^{17}	*0.4/124.9*	*0.5/125.8*	*2.3/133.4*
1×10^{18}	*0.4/128.9*	*0.5/134.7*	*1.8/134.6*

F. Summary of Ballute Static Analysis

The deformed shape of a ballute was calculated at two points on a Titan aerocapture trajectory, one at peak dynamic pressure (using

Table 6 Computational domain dimensions and axial force using the Fine grid with 1×10^{15} RTS molecules

Domain no.	1	2	3	4	5	6	7	8
Domain width, m	15	15	15	20	20	20	20	25
Axial length, m	11	13	15	19	25	28	32	32
Axial force, N	132.0	126.5	123.1	120.7	118.9	118.5	118.2	118.4
Change in axial force	——	4.2%	2.7%	2.0%	1.5%	0.3%	0.3%	0.2%

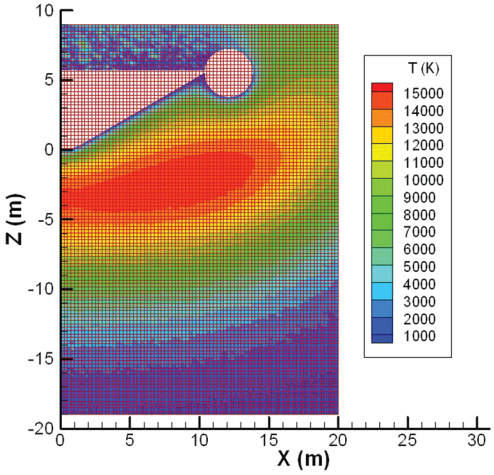

Fig. 34 Flowfield temperature in domain size 6.

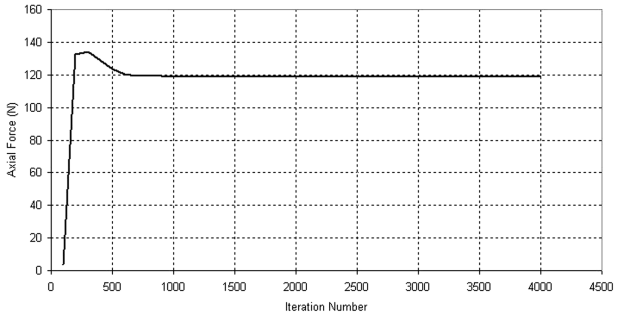

Fig. 35 Converged forces on the final coupling iteration for DAC.

modified Newtonian analysis and NASCART-GT) and the other in the transitional regime (using collisionless DSMC and DAC). The resulting deformation and stress indicate that the ballute could survive the flight environment. Heating and accurate surface temperature prediction at these points requires further analysis.

Using continuum methods at the peak dynamic pressure point, there was good agreement between the low- and high-fidelity models for drag and stresses. Axial displacement of the torus, however, was different by 69%, though this had little affect on the other metrics. Considering the computational time difference, the low-fidelity analysis provides sufficient accuracy for conceptual design studies where drag and von Mises stress prediction of the deformed shape are sufficient.

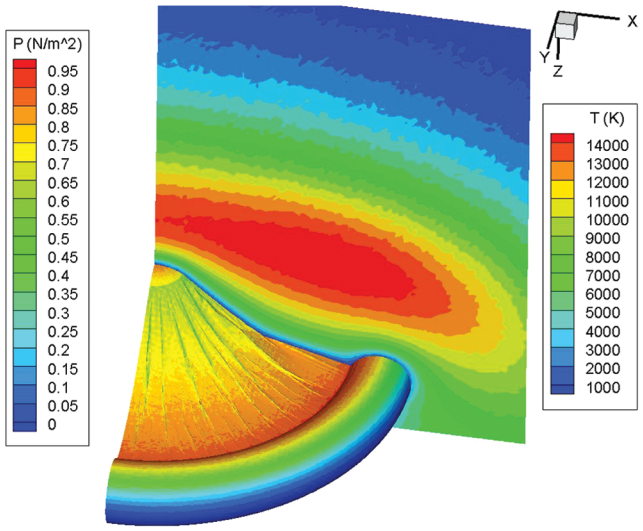

Fig. 36 The deformed clamped ballute in the transitional regime with surface pressure contours in Pa and flowfield temperature in Kelvin.

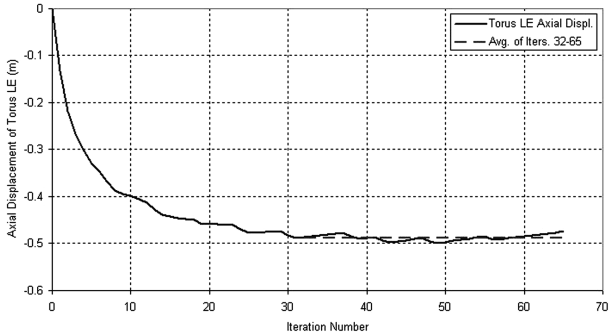

Fig. 37 Axial displacement of the torus after each coupling iteration. Forward displacement is negative.

Comparison of the impact method aerodynamics and DSMC in the transitional regime indicate that the impact method is sufficient for trajectory analysis (drag prediction 13% lower for low-fidelity methods on this configuration) but not for determining static stresses. The low total load at this point on the trajectory and the low stresses indicate that this point is not a design driver, and so only drag information from this point would be of interest during conceptual design.

From a conceptual design perspective, the parameters of interest (peak stress on the trajectory and drag at each point) are represented with sufficient accuracy by the low-fidelity methods for this configuration. When computation time is considered, the low-fidelity solutions provide a good compromise of time and accuracy.

V. Conclusions

This research effort has developed the variable-fidelity ballute aeroelastic analysis tool (BAAT), an aeroelastic design framework for thin-film ballutes. The code uses LS-DYNA for structural analysis and obtains aerodynamic pressures from either NASCART-GT, DAC, or impact methods, depending on the fidelity desired and the flight regime.

BAAT was validated using wind-tunnel test data from a 6-in. diam flexible Kapton model in the hypersonic CF_4 wind tunnel at Mach 5.6. The deformed shape of the vehicle forebody was predicted using both low- and high-fidelity analyses in the continuum regime. During the solution process it was found that the deformed shape was more sensitive to structural parameters than to the aerodynamic load distribution. The computed deformed shape using both the low- and

Table 7 Metrics for the clamped ballute at peak dynamic pressure

Metric	Mod. Newtonian	CFD	Difference
Axial deflection of torus, m	0.13	0.079	69%
Max. von Mises stress, MPa	37.1	38.9	4.8%
Max. strain, %	0.39	0.55	40%
Nose pressure, Pa	94	89	5.6%
Drag, N	10,662	11,493	8%
Approximate computation time[a]	23 h	5 days	420%

[a]CFD uses 21 AMD Opteron 248 cores and FEA uses 31 cores.

Table 8 Metrics for the clamped ballute in the transitional regime

Metric	Collisionless DSMC	DSMC	Difference
Axial deflection of torus, m	−0.7	−0.47	49%
Max. von Mises stress, MPa	22.5	6.5	246%
Max. principal stress, MPa	13.6	7.5	81%
Max. strain, %	0.39	0.06	5.5%
Nose pressure, Pa	0.80	0.83	3.8%
Drag, N	105.0	118.7	13%
Approx. computation time[a]	15 hrs.	22 days	3570%

[a]Time using 32 AMD Opteron 248 cores.

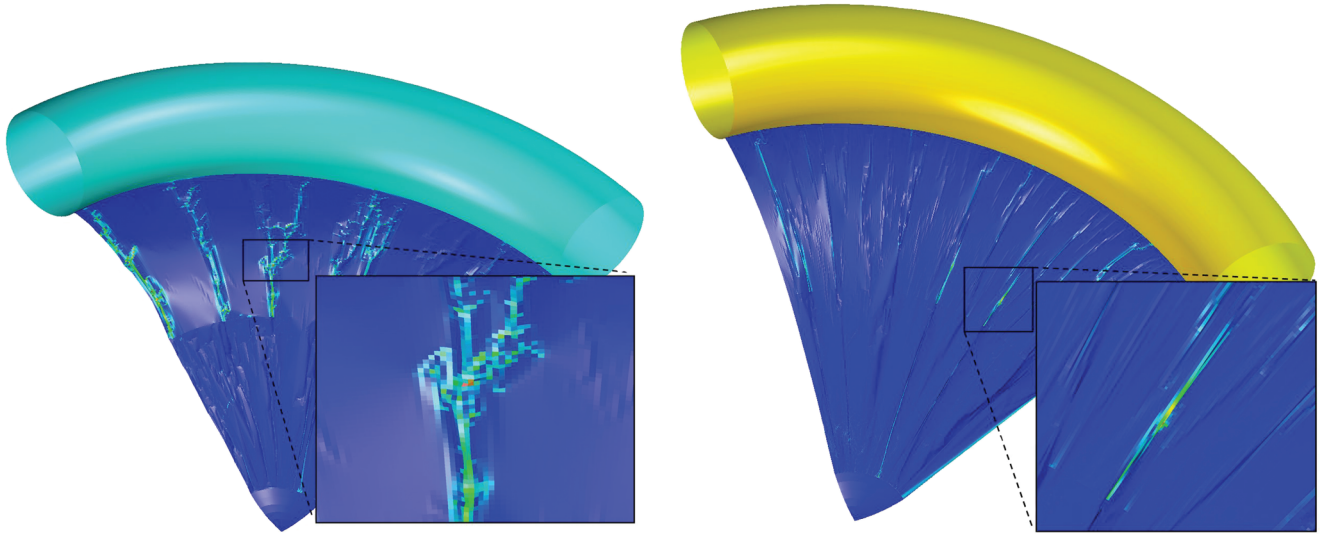

a) Low-fidelity model b) High-fidelity model

Fig. 38 Peak stress location and wrinkle shape differs between the low- and high-fidelity models in the transitional point analysis.

high-fidelity analyses matched the experiment very well for the wind-tunnel test model.

High-fidelity analysis solutions of a clamped ballute were computed at two conditions on a Titan aerocapture trajectory using NASCART-GT or DAC coupled to LS-DYNA. The flight conditions selected were at the peak dynamic pressure point (continuum regime) and in the high transitional regime just after encountering the atmosphere. These solutions represent the first published aeroelastic solutions of a thin-film ballute using inviscid, perfect gas aerodynamics.

Low-fidelity solutions were computed and compared to the high-fidelity analysis at the same two points on a Titan aerocapture trajectory using a thin-film clamped ballute. Analysis at the peak dynamic pressure point showed good agreement of stresses and drag, despite a nearly 70% difference in axial displacement of the torus. The difference was attributed to a difference in load distribution on the torus that resulted in only an 8% difference in drag. Analysis at the transitional point produced drag within 13% for the low- and high-fidelity results, but a large discrepancy in predicted stresses and torus displacement. From a design perspective, the large discrepancy in predicted stresses and torus displacement is not a problem because the stresses at this point do not drive structural considerations, and the drag prediction is within reason (despite the difference in deformed shape) for use in conceptual design. Furthermore, the low-fidelity analysis is between 4 and 35 times faster than comparable high-fidelity analysis (depending on the flight regime).

The analysis presented shows that low-fidelity analysis is sufficient to predict the peak stress on the trajectory and the drag along the trajectory for conceptual design of the thin-film clamped ballute geometry studied. When the analysis time is compared relative to the accuracy gained, the low-fidelity analysis methods are especially attractive.

From a conceptual design prespective, both the low- and high-fidelity analysis presented indicates that the thin-film clamped ballute studied could survive the Titan aerocapture environment from an aeroelasticity perspective. The peak stress level is well below the ultimate stress of Upilex, and no buckling is observed.

References

[1] Andrews, D., and Bloetscher, F., "Aerobraked Orbital Transfer Vehicle Denition," AIAA Paper 81-0279, 12–15 Jan. 1981.

[2] Grenich, A., and Woods, W., "Flow Field Investigation of Atmospheric Braking for High Drag Vehicles with Forward Facing Jets in Spacecraft Entry," AIAA Paper 81-0293, 12–15 Jan. 1981.

[3] McRonald, A., "A Light-Weight Inflatable Hypersonic Drag Device for Venus Entry," AAS Paper 99-355, 16–19 Aug. 1999.

[4] Rohrschneider, R., and Braun, R., "Survey of Ballute Technology for Aerocapture," *Journal of Spacecraft and Rockets*, Vol. 44, No. 1, 2007, pp. 10–23. doi:10.2514/1.19288

[5] Hall, J., "A Review of Ballute Technology for Planetary Aerocapture," IAA Paper IAA-L-1112, 2–5 May 2000.

[6] Baum, J., Lua, H., Mestreau, E., Sharov, D., Lohner, R., Plessone, D., and Charman, C., "Recent Developments of a Coupled CFD/CSD Methodology," AIAA Paper 2001-2618, 11–14 June 2001.

[7] Matthies, H., and Steindorf, J., "Partitioned Strong Coupling Algorithms for Fluid-Structure Interaction," *Computers and Structures*, Vol. 81, Nos. 8–11, 2003, pp. 805–812. doi:10.1016/S0045-7949(02)00409-1

[8] Bhardwaj, M., Kapania, R., Reichenbach, E., and Guruswamy, G., "Computational Fluid Dynamics/Computational Structural Dynamics Interaction Methodology for Aircraft Wings," *AIAA Journal*, Vol. 36, No. 12, 1998, pp. 2179–2186.

[9] Bauchau, O., and Ahmad, J., "Advanced CFD and CSD Methods for Multidisciplinary Applications in Rotorcraft Problems," AIAA Paper 96-4151, 4–6 Sept. 1996.

[10] Livermore Software Technology Corp., "*LS-DYNA Keyword User's Manual*, 970th ed., Livermore Software Technology Corporation, Livermore, CA, 2003.

[11] Topping, A., "Ring Buckling of Inflated Drag Bodies," *Journal of Aircraft*, Vol. 8, No. 11, 1970, pp. 869–874.

[12] Marshall, D., and Run, S., "A New Inviscid Wall Boundary Condition Treatment for Embedded Boundary Cartesian Grid Schemes," AIAA Paper 2004-0583, 5–8 Jan. 2004.

[13] Tu, S., and Run, S., "Solution Adaptive, Unstructured Cartesian-Grid Methodology for Chemically Reacting Flows," AIAA Paper 2002-3097, 24–26 June 2002.

[14] LeBeau, G., and Lumpkin, F. E. I., "Application Highlights of the DSMC Analysis Code (DAC) Software for Simulating Rarefied Flows," *Computer Methods in Applied Mechanics and Engineering*, Vol. 191, Nos. 6–7, 2001, pp. 595–609. doi:10.1016/S0045-7825(01)00304-8

[15] Bird, G., *Molecular Gas Dynamics and the Direct Simulation of Gas Flows*, Oxford Univ. Press, New York, 1994.

[16] Anderson, J. D. J., *Hypersonic and High Temperature Gas Dynamics*, AIAA, Reston, VA, 2000.

[17] Wilmoth, R., Blanchard, R., and Moss, J., "Rarefied Transitional Bridging of Blunt Body Aerodynamics," *21st International Symposium on Rarefied Gas Dynamics*, July 1998.

[18] Miller, K., Gulick, D., Lewis, J., Trochman, B., Stein, J., Lyons, D., and Wilmoth, R., "Trailing Ballute Aerocapture–Concept and Feasibility Assessment," AIAA Paper 2003-4655, 20–23 July 2003.

[19] Moss, J., Blanchard, R., Wilmoth, R., and Braun, R., "Mars Pathfinder Rarefied Aerodynamics: Computations and Measurements," AIAA Paper 98-0298, 12–15 Jan. 1998.

[20] Buck, G., "Testing of Flexible Ballutes in Hypersonic Wind Tunnels for Planetary Aerocapture," AIAA Paper 2006-1319, 9–12 Jan. 2006.

[21] "Summary Properties for Kapton Polyimide Films," DuPont Corp.,

TR H-38492-1, March 1997.
[22] Stroud, W., and Zender, G., "Experimental Investigation to Determine Utility of Tension Shell Concept," NASA TR NASA-TM-X-1211, March 1966.
[23] Morley, C., "GasEQ: A Chemical Equilibrium Program," 0th ed., http://www.gaseq.co.uk [retrieved March 2007].
[24] Miller, K., Masciarelli, J., Hausle, F., Riesco, M., Sharma, D., Zeller, C., Gnoffo, P., Buck, G., Ware, J., and Rohrschneider, R., "Ultralightweight Ballute Technology for Aerocapture and Aeroassist Missions," NASA TR NASA/CR-2008-215248, Jan. 2007.
[25] Johnson, W., and Lyons, D., "Titan Ballute Aerocapture Using a Perturbed TitanGRAM Model," AIAA Paper 2004-5280, 16–19 Aug. 2004.
[26] Westhelle, C., and Masciarelli, J., "Assessment of Aerocapture Flight at Titan Using a Drag-Only Device," AIAA Paper 2003-5389, 11–14 Aug. 2003.
[27] Brown, G., and Richardson, E., "Minimum-Mass Design for Titan Aerocapture," AIAA Paper 2005-1637, May 2005.
[28] James, B., Munk, M., and Moon, S., "Aerocapture Technology Project Overview," AIAA Paper 2003-4654, 20–23 July 2003.
[29] Van der Heide, E. J., Kruij, M., Avanzini, A., Liedtke, V., and Karlovsky, A., "Thermal Protection Testing of the Inflatable Capsule for YES2," IAC Paper 03-I.3.05, 29 Sept.–3 Oct. 2003.

L. Peterson
Associate Editor